

Wettability and Corrosion Behavior of Chemically Modified Plasma Electrolytic Oxidation Nanocomposite Coating

S.S. Farhadi, M. Aliofkhaezai, Gh. Barati Darband, A. Abolhasani, and A. Sabour Rouhaghdam

(Submitted May 10, 2016; in revised form June 20, 2017; published online September 21, 2017)

The aim of this paper was to investigate the effect of potassium stearate on the wettability behavior, corrosion resistance, roughness and thickness of reinforced and unreinforced plasma electrolytic oxidation (PEO) coatings with Si_3N_4 nanopowders. Morphological characteristic, corrosion behavior and wetting properties of the coatings were evaluated using SEM, cyclic polarization and Wilhelmy plate method, respectively. In order to obtain a better evaluation of the contact angle, roughness of the coatings was studied by AFM. The results indicated that the nanocomposite hydrophobic coatings have the best corrosion resistance. Potassium stearate could repel water from the holes of coating by reacting with aluminum and producing aluminum stearate. The contact angle of nanocomposite and normal PEO coatings was increased up to 65° due to the addition of potassium stearate. This additive could also increase the hysteresis contact angle up to 51° .

Keywords corrosion resistance, plasma electrolytic oxidation, wettability, Wilhelmy plate

1. Introduction

Metals are coated for many purposes such as improving their corrosion, abrasion and high-temperature resistance, biocompatibility and wettability properties. In turn, wettability properties involve the issues such as self-cleaning (Ref 1), heat transfer (Ref 2), super-hydrophobicity (Ref 3), anti-icing (Ref 4), tribology (Ref 5), anti-fouling (Ref 6) and absorbing liquids like oil. In this regard, inspiring from the natural models (e.g., plants), many efforts have been made to create hydrophobic surfaces on metals. The “super-hydrophobic” concept was originally derived from lotus leaf in the nature, which is known as “lotus effect.” Water-repellent and self-cleaning properties of these surfaces are attributed to the lotus effect, which indeed is a combination of water-wax repellency effect and the surface roughness obtained from the hierarchical structures (Ref 7). Although many papers have been published on theoretical simulation and modeling of contact angle, researchers have mainly worked on the practical aspects of this phenomenon, in order to develop simple methods of fabricating such surfaces with lower expense and more durability. Fabrication of hydrophobic coatings involves single- or multi-step methods. These methods are all based on mimicking from the nature and the two principles of surface roughening and decrease in surface tension. Here, the most common methods are electro-

chemical deposition (Ref 8, 9), plasma treatment (Ref 10), chemical vapor deposition (CVD) (Ref 11), sol-gel techniques (Ref 12) and immersion (Ref 13, 14). Some recent works have provided the required roughness for hydrophobic coatings through anodizing and adjusting the surface tension of the coating by applying organic compounds such as silanes (Ref 15, 16) and polymers (Ref 17). These coatings represent a superior resistance to corrosion owing to the high thickness of the anodized layer (Ref 18, 19).

PEO is a process in which substrates are coated in an alkaline electrolyte at a constant electrical current and electrical discharge occurs in the breakdown potential of the formed oxide film. This electrical discharge leads to the formation of plasma between the substrate and the electrolyte, which in turn can create melted oxide after the reaction. After contacting with the liquid electrolyte, the melted oxide is quickly cooled, and using the SEM images, it is possible to observe the location of the last discharges. The sparks induced by these electrical discharges can attract the nanopowders suspended in the electrolyte and keep them inside the coating and create nanocomposite coating. Here, the breakdown potential is influenced by the salts dissolved in the electrolyte. Besides, the chemical composition of the dissolved salt can affect the intensity and number of sparks. Another role of the salts added to the electrolyte is to supply oxygen content needed for the oxidation process. Plasma electrolytic oxidation (PEO) facilitates creation of single-layer and multilayer nanocomposite coatings (Ref 20). PEO coating has hydrophilic surface so it is wetted by water. If the surface repels the molecules of water and a droplet of water forms a spherical shape, the water contact is minimized and the surface is called hydrophobic. Roughness of the hydrophobic surface can increase the contact angle. Wenzel model explains a mode in which water and surface contacted during the increase in roughness (Ref 7). Cassie-Baxter model explains a situation wherein air is trapped in the surface. Air trapping increases the contact angle and makes the surface super-hydrophobic (Ref 7).

S.S. Farhadi, M. Aliofkhaezai, Gh. Barati Darband, A. Abolhasani, and A. Sabour Rouhaghdam, Department of Materials Science, Tarbiat Modares University, P.O. Box 14115-143, Tehran, Iran. Contact e-mails: alioftmu2@gmail.com, maliofkh@gmail.com and khazraei@modares.ac.ir.

In a one-step procedure and by using the PTFE suspension in the electrolyte, this method creates a thick single-layer hydrophobic coating on the aluminum, magnesium and titanium substrates (Ref 21, 22). Shift of the corrosion potential toward more noble values and reduction of the corrosion rate are the result of these PTFE-containing coatings. PEO can be applied as a preprocessing for another coating process to create the desired wetting angle on the coating. The hydrophobic coating is developed in a multi-step approach by deposition of a silane-based nanocomposite layer on the PEO coating (Ref 23, 24). The one-step hydrophobic coating was first fabricated by adjustment of the electrolyte of anodizing process (Ref 25). In other studies, saturated fatty acids have also been used in a two-step procedure after anodizing (Ref 26, 27). The electrolyte used in this study contained saturated fatty acids with hydroxyl branch, which can stick to the surface, where the other terminal of the chain makes the surface hydrophobic. Note that these fatty acids can affect the contact angle if converted into a compound, which can be suspended in the PEO electrolyte. The aim of this study is to fabricate a hydrophobic coating using one-step treatment. In this regard, potassium stearate was added to the electrolyte, and the effect of potassium stearate concentration and nanoparticle concentration on the microstructure, wettability behavior and corrosion behavior of the coatings was investigated.

2. Experimental Procedure

2.1 Materials

The variables in this work are additives concentration and nanopowders concentration. The coating process was carried out on commercial aluminum alloy 1190 substrate (Fe: 0.15%, Si: 0.05%, Mn: 0.02%, and Cu: 0.01%). The samples were washed in 10 wt.% NaOH solution before the coating process and prepared in coupon form with the dimensions of 3 cm × 3 cm × 0.1 cm. A PEO coating rectifier with 20 KW power with stainless-steel cathode was used for the electrochemical coating process. Potassium stearate was synthesized through the neutralization of KOH with stearic acid (Merck) in the water-based solution considering the corresponding stoichiometry ratio. Because of its long 18 carbon chain, stearate acid is insoluble in water; so to prevent its transformation to gel, the electrolyte must be kept at temperatures above 80 °C. Si₃N₄ nanopowders with an average grain size of 37 nm were suspended in the electrolyte. Figure 1 shows the TEM image of these nanopowders captured using CM-180 Philips TEM apparatus. Aqueous sodium silicate solution with the concentration of 4 g/l was used as an electrolyte. Potential variations during the coating were recorded using an APPA multimeter (model: 505) connected to a computer and with a scanning rate of 0.5 s. Due to the opacity of the electrolyte caused by the addition of nanopowders, and consequently, lack of proper sight on the sparks for record of voltage of sparking initiation, sparking voltage was assumed as 400 V (sparking voltage without nanopowder sample). The coating process proceeded by selecting two different types/values for each variable, i.e., electrolyte and concentration of additive and nanopowder (Table 1). Coating period was selected as 10 min, and minimum sparking current density (DC mode) was selected to be 22 mA/cm².

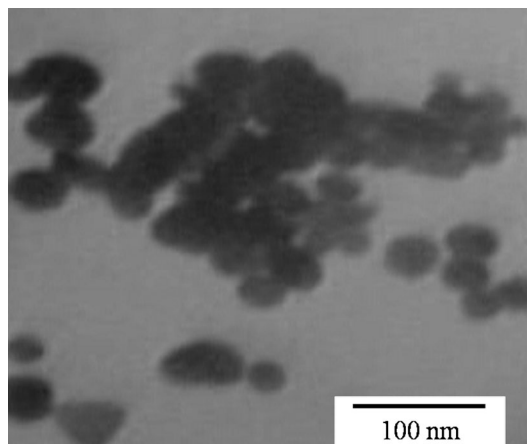


Fig. 1 TEM image of Si₃N₄ nanoparticles

Table 1 Composition and coating conditions of the samples

Sample code	Concentrate of nanopowder, g/l	Concentrate of additive, g/l
S-0-2	0	2
S-0-4	0	4
S-5-2	5	2
S-5-4	5	4
R-0-0	0	0
R-5-0	5	0

2.2 Evaluation Methods

2.2.1 Thickness and Weight. All specimens were weighted before and after the coating process using AND-GR202 scale with the precision of 50 µg. It is to be noted that just before weighing the specimens, they were carefully rinsed and dried. Thickness of the coatings was reported with the mean value of 10 measurements using the Qnix thickness gauge (model: P5800).

2.2.2 Microstructure and Composition. The linear profiles of the surface roughness of all coatings were obtained by the roughness test gauge of Taylor Hobson Surtronic 25. To characterize the surface morphology of the samples, scanning electron microscope (SEM) (model Sigma/VP, ZEISS, Germany and XL30, Phillips, Netherland) was used. Zeiss microscope (model: EM 900) was used to capture the TEM images of the coatings. Surface element analysis was carried out using the EDS method by FESEM microscope (Sigma/VP of ZEISS). Surface topography of the samples was prepared using the ARA-AFM device with a scanning area of 30 µm × 30 µm and the scanning rate of 0.05 line per second. Surface porosity percentage of the coatings was calculated using “ImageJ” software. The infrared spectra of the coatings were recorded by FTIR spectrometer (Spectrum 100, PerkinElmer).

2.2.3 Wettability. To evaluate wettability of the coatings, the two concepts of contact angle and hysteresis of contact angle should be measured. For this purpose, all wettability tests were carried out using the DI water. Dino-Lite AM413ZT digital microscope instrument was used to take pictures from the spreading drops. To calculate static contact angle, using a

handmade system, 10 μl of DI water drops was dripped on the surface of the coatings. Then, the arc angle (the central angle of the arc in degrees) above the interface was measured, which equals to the sum of two interior angles, using “image analyzer” software. The reported static contact angle was the mean value of six drops on each coating. Hysteresis contact angle was obtained using the Wilhelmy plate method.

Wilhelmy plate balance (homemade by AND-GR202 balance) worked at the immersion and withdrawal speeds of 160 $\mu\text{m/s}$. The plate was suspended, pendulum-like, via steel wire with an alligator clip. The wire was bent slightly prior to the commencement of a run so as to ensure that the plate entered the liquid perpendicularly to the surface. At this point, the immersion depth, time and force measurements were set to zero, and continuous recording commenced. Data acquisition test was performed at a rate of 2 points/s using AND software. Contact angle calculation of Wilhelmy plate was reported elsewhere (Ref 28). Contact angle is calculated by the following formula at zero immersion depth:

$$F = P \times \gamma_l \times \cos \theta \quad (\text{Eq 1})$$

where F is force, γ_l is surface tension (N/m) of water, P is perimeter of wetting (m) and θ is contact angle.

The liquid contact angle on the flat surface (θ_{flat}) can be correlated with three interfacial free energies, i.e., free energies at the solid–air (γ_{sv}), solid–liquid (γ_{sl}) and liquid–air (γ_l) interfaces, by the Young’s equation:

$$\gamma_{\text{sv}} = \gamma_{\text{sl}} + \gamma_l (\cos \theta_{\text{flat}}) \quad (\text{Eq 2})$$

Solution of linear system with two variables needs two equations. So calculation of surface tension needs two liquids by different contact angles. The advancing and receding contact angles obtained using the Wilhelmy force were converted to the surface tension using the Chibowski formula (Ref 29). Chibowski formula is valid in Wenzel model wettability:

$$\gamma_{\text{sv}} = \gamma_l \left(\frac{(1 + \cos \theta_a)^2}{2 + \cos \theta_r + \cos \theta_a} \right) \quad (\text{Eq 3})$$

where γ_{sv} is the surface tension of solid/air interface, γ_l is the surface tension of liquid, θ_a is the advancing contact angle, and θ_r is the receding contact angle. Chibowski formula has one variable (the surface tension of liquid) so surface tension at the solid/air interface is obtained through calculating the hysteresis contact angle of single liquid (water).

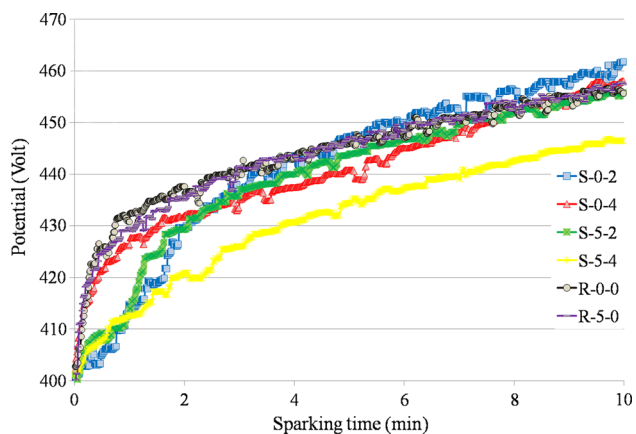


Fig. 2 Voltage–time curves for various samples

2.2.4 Corrosion Behavior. The electrochemical corrosion test was conducted in 3.5 wt.% NaCl solution. The corrosion resistance of the coatings was studied through the cyclic polarization method using the potentiostat/galvanostat apparatus (EG&G-273A). Thirty minutes was needed for the open-circuit potential of coating to be constant. Then, the samples were subjected to the cyclic polarization within -0.4 to $+2.0$ volts to the open-circuit potential (OCP), and finally, were returned to the OCP condition. The corrosion test was performed at the scanning rate of 1 mV/s and the scanning height of 2 mV/s. As the reference electrode, a calomel electrode was used. The data of corrosion test were obtained using the “Powersuit v. 2.5” software.

3. Results and Discussion

3.1 Voltage–Time Diagram

Figure 2 illustrates the voltage–time diagram during the sparking for normal and nanocomposite samples, and Table 2 shows the spark voltage during the sparking treatment. A comparison between the typical samples (R-0-0 and R-5-0) indicates that the samples without additive do not show any significant difference in spark initiation voltage even after the addition of nanopowders. This implies that, in the absence of an additive, no alteration in the coating mechanism has occurred with the addition of nanopowders. This conclusion has also been observed by other investigators (Ref 30, 31). Moreover, comparing samples S-0-2 and S-0-4 with sample R-0-0 indicates that the addition of potassium stearate to the electrolyte has reduced the sparking voltage’ rise rate in the early minutes of the coating process. Sample S-0-2 has compensated this reduction after 4 min of coating as it exhibited higher ultimate voltage comparing with the other samples. Sample S-0-4 represented a behavior similar to that of sample R-0-0, involving fewer volts in the sparking voltage as the additive content of the electrolyte increases. Rate of sparking voltage rise at constant current for sample S-0-4 is similar to that of the sample without additive, where their ultimate voltages have almost a 5-V difference.

Comparison of S-5-2 and S-5-4 samples with sample R-5-0 shows that the addition of potassium stearate to the electrolyte of nanocomposite coating leads to decrease in the rate of sparking voltage rise at the early minutes of the coating process. This behavior is similar to that resulting from adding potassium stearate to the electrolyte of the coating without nanoparticles. The addition of 2 g/l of potassium stearate to the electrolyte of the nanocomposite coatings has decreased the rate of sparking voltage rise at the beginning; however, at the higher sparking times, this rate was approximately equal to that of the samples without additive (comparison between S-5-2 and R-5-0 samples). In the S-5-4 sample, about 12 volts reduction in sparking voltage is related to increase in the conductivity of the electrolyte with increase in the concentration of the potassium stearate. At the same concentration of additive, a comparison of the curves related to the normal (S-0-2, S-0-4) and nanocomposite (S-5-2, S-5-4) samples revealed that the decrease in sparking voltage has happened during the coating process with the addition of nanopowders, which is in agreement with the results of other researchers (Ref 32–35). Growth of coating during the PEO process in the presence of nanoparticles has a

Table 2 Characteristics of potential–time curve, thickness, roughness and porosity of the coatings

Sample code	Finish voltage, V	$V_{\text{final}} - V_{\text{sparking}}$, V	Joule/cm ²	Coating thickness, μm	Weight change, %	Surface porosity, %
S-0-2	461	61	5812	1.1	-0.041	3
S-0-4	453	53	5798	0.2	0.984	2
S-5-2	455	55	5799	2.8	2.906	1
S-5-4	446	46	5689	1.0	2.930	1
R-0-0	457	57	5857	0.9	-0.541	5
R-5-0	458	58	5855	1.5	1.360	4

complex pattern, and many reactions occur near the surface of the substrate. It is difficult to describe all of the reactions, but decrease in the sparking voltage agrees with the finding of other researchers (Ref 36).

3.2 Weight Change of Coating

Weight changes of coatings in different conditions are represented in Table 2. Generally, PEO coating formation consists of weight reduction due to the dissolution of substrate and weight gain due to oxide formation on the substrate. As it can be seen, sample R-0-0 represents a weight reduction of 0.5%. It means that the rate of substrate dissolution and entrance of ions into the electrolyte is more than the rate of oxide formation, whereby mass has reduced. Comparison of samples R-0-0 and R-5-0 shows that the addition of nanopowders to the electrolyte has led to 1.3% increase in mass and made the rate of coating fabrication more than the rate of dissolution of substrate. Also comparison of the weight changes of samples S-5-2 and S-5-4 with sample R-5-0 shows that adding potassium stearate to the electrolyte has compensated the weight loss of sample S-0-2 and brought it nearly to zero and for sample S-0-4, it increased the weight change to + 1%. Increase in the weight of samples with additive is attributed to the deposition of stearate chains. Comparison of the weight changes of samples S-5-2, S-5-4 to sample R-5-0 reveals that the presence of additive in both concentrations has led to increase in the weight gain of nanocomposite coatings from 1.3 to 2.9%. At the same concentration of additive, nanocomposite samples (S-5-2, S-5-4) represent a higher weight gain than normal samples (S-0-2, S-0-4). Nanopowders' absorption in the coatings is also attributed to this higher weight gain (Ref 37, 38). Both factors (additive and nanopowders) have increased weight gain of the samples. The maximum change (2.93%) related to sample S-5-4 is because of the synergistic effect of the aforementioned factors.

3.3 Microstructure and Morphology of Coatings

Figure 3 shows the surface SEM images of the samples coated at different conditions. Table 2 reports the porosity percentage on the top surface of the samples. As can be seen, the surface of coatings has several microspores that are distributed uniformly in the entire surface.

Sparking causes the decomposition of water (H_2O) into hydrogen gas (H_2) and oxygen gas (O_2). It is believed that the cause of microspore formation is the evolution of anodic gases (oxygen) evolved on aluminum (during plasma formation) through molten materials due to the coatings growth processes. The molten products in the vicinity of volcano-like pores indicated that the plasma temperature at the surface of Al alloy is very high during the plasma electrolytic oxidation process.

By comparing the results of the porosity percentage of samples R-0-0 and R-5-0, it is found that the addition of nanopowders to the electrolyte has decreased the pore content from 5 to 4%. Comparison of the porosity percentage of samples S-0-2 and S-0-4 to sample R-0-0 reveals that adding potassium stearate to the electrolyte at 2 and 4 g/l concentration has reduced the porosity of the coating by almost 3 and 2%, respectively. A comparison of the porosity percentage of samples S-5-2 and S-5-4 to sample R-5-0 shows that in the presence of nanopowders, two concentrations of potassium stearate could reduce the surface porosity to its minimum value (1%). Reduction of the surface porosity of coatings due to the presence of nanoparticles has been also reported elsewhere (Ref 39-41). Therefore, sample S-5-4, which has the highest content of additive and nanopowder, has the lowest porosity and surface holes (Fig. 3d). Porosity decline may have a significant effect on the decrease in corrosion rate, which will be discussed in the following sections. Figure 4 shows the photograph of a cross section of nanocomposite coating related to the sample S-5-2 taken by a transmission electron microscope. A matrix of amorphous aluminum oxide and dispersed silicon nitride particles is observed in Fig. 4. Figure 5 shows the results of EDS analysis performed on the surface of nanocomposite samples with additive. In both samples (S-5-2, S-5-4), it is seen that the content of aluminum element around the cavities has risen, showing the emission of x-ray spectra from the substrate because of the thin coating. Other elements are distributed uniformly on the surface of the nanocomposite coating in the presence of additive. Uniform distribution of elements on the surface indicates that all phases are distributed uniformly, and the resultant properties of these coatings are independent of phase dispersion. The presence of elements originating from the electrolyte and those from the substrate in the elemental mapping of surface indicated the incorporation of electrolyte element and substrate element into the coating formation process.

Figure 6 illustrates the results of the coatings' surface roughness obtained from the AFM test and the calculated R_a via the linear roughness gauge. A comparison between the surface roughness of samples R-0-0 and R-5-0 in Fig. 5 reveals that the addition of nanopowder to the sample results in no change in the range of height variation parameter in the surface roughness, which leads to 0.1 μm drop in R_a value. Comparison of the roughness of samples S-0-2 and S-0-4 and sample R-0-0 implies that the addition of potassium stearate to the electrolyte shifts R_a to 0.2 for 2 g/l concentration and 0.1 for 4 g/l concentration. Also, the comparison of the roughness values for sample S-5-2 with those of other samples reveals that although nanopowder decreases roughness (Ref 42), the higher concentrate of potassium stearate with nanopowder increases R_a up to 0.8 μm . Based on the literature (Ref 43-45), surface roughness alone is not enough to make a significant change in contact

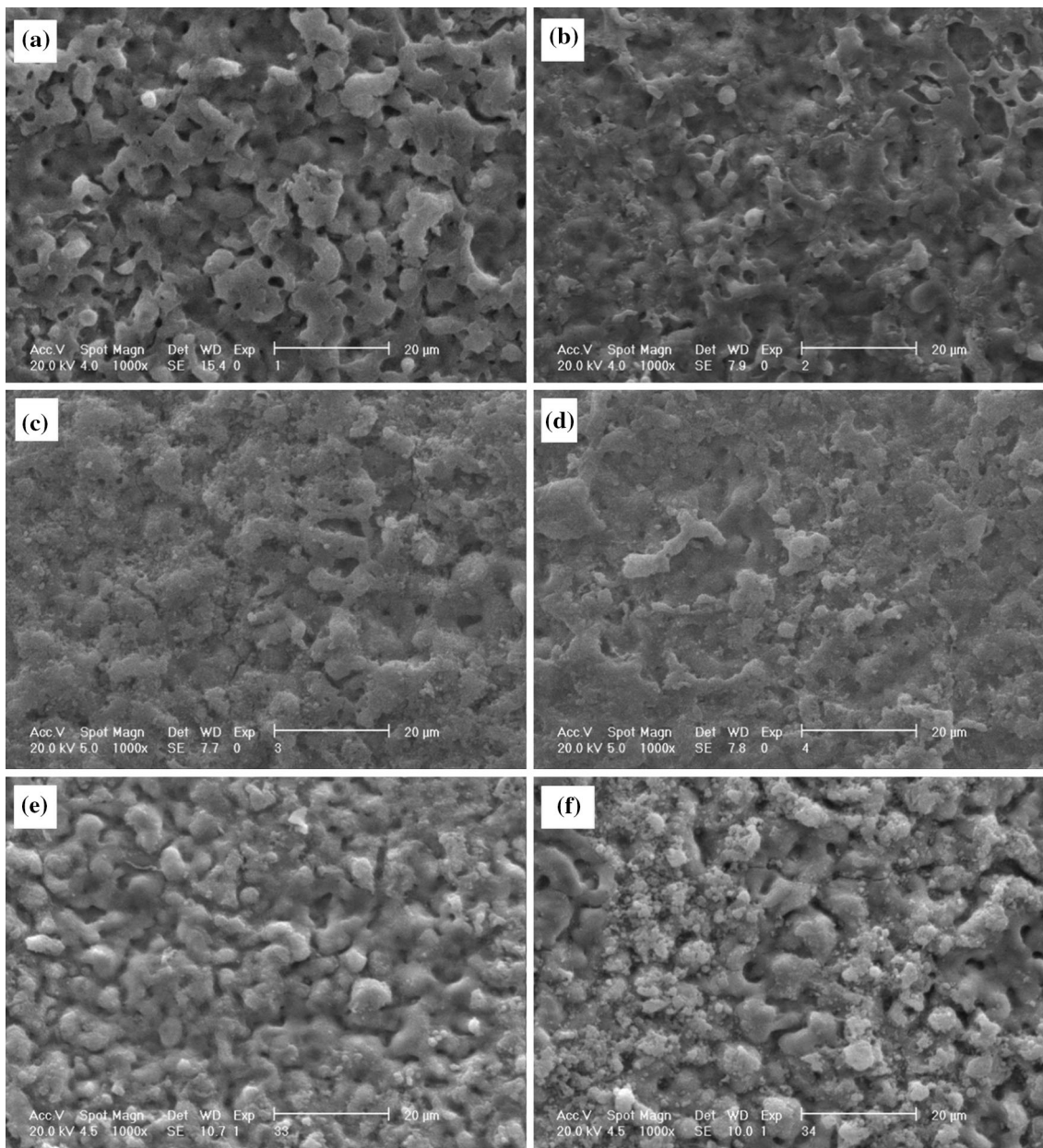


Fig. 3 SEM micrograph of the free surface of samples, showing (a) S-0-2, (b) S-0-4, (c) S-5-2, (d) S-5-4, (e) R-0-0, and (f) R-5-0

angle; surface tension is another factor that affects contact angle.

3.4 Wettability Behavior

Figure 7 shows the curves of Wilhelmy plate force versus immersion depth for various samples, and Table 3 presents the contact angle values resulting from static drop, the hysteresis of the contact angle from the samples shown in Fig. 7, and the surface tension calculated using the Chibowski equation. One condition needed for validation of Chibowski equation is Wenzel's wettability model on surface. Thus, Chibowski equation (Ref 46) was applied for calculation of surface tension on the free surface of coatings. The advancing and receding contact angles of the coating were used to estimate the surface tension in Chibowski equation. As listed in Table 3, due to complete wetting of the samples, the receding contact angles in

Wilhelmy test are almost equal. The static contact angle for the additive-free samples (R-0-0 and R-5-0) is 6°, indicating that the surface of PEO coating in the sodium silicate-based electrolyte has a hydrophilic nature. Using the Wilhelmy plate method, the receding contact angle for samples R-0-0 and R-5-0 was estimated to be 30°. For the small contact angles, the liquid has positive concavity, and the contact angle calculated by the Wilhelmy plate method is bigger than the real contact angle because of the Vander Waals and electrostatic double-layer forces (Ref 47). As a result, the real receding contact angle of both samples is more than 30°. Such increase, in turn, results in 2 mN/m² (≈ 3%) reduction in the surface tension. Because of the complete wetting, using the Wilhelmy force method, the receding angles of various samples are almost equal, while the maximum difference was observed in the advancing angle. A comparison between the wettability results of samples R-0-0 and R-5-0 indicates that the addition of

nanopowders to the additive-free sample results in the increase in hydrophilic properties because of the hydrophilic nature of nanoparticles and the increase in the Wilhelmy force curve of sample R-5-0. Here, the nanocomposite coating indicates a lower hysteresis of contact angle in comparison with the normal sample. A comparison of the wettability results of samples S-0-2 and R-0-0 indicates that the addition of potassium stearate to the electrolyte of normal coatings results in 6° to 65° increase in the contact angle and a decrease in the hydrophilic property of the surface. The advancing contact angle of sample S-0-2 rises up to 90°, and the sample inclines to convert into hydrophobic nature. Advancing and receding contact angles calculated using the Wilhelmy plate method showed that the hysteresis of the contact angle is equal to 51°. The addition of potassium stearate

to the electrolyte of normal coatings results in 50% drop in the surface tension compared to sample R-0-0. However, a comparison between the wettability results of samples S-0-2 and S-0-4 showed that the concentration of additive has an inverse relation to the contact angle, where it brings the static contact angle to 40°, and the advancing contact angle to 79°. In this regard, sample S-0-4 shows 44% drop in the surface tension compared with sample R-0-0.

Comparison between the wettability results of samples S-5-2 and R-5-0 indicates that the addition of potassium stearate to the electrolyte of nanocomposite coating also results in the corresponding 39° rise in the static contact angle and 77° rise in the advancing contact angle. Here, sample S-5-2 has 46% drop in the surface tension compared with sample R-5-0. In addition, by comparing the wettability results of samples S-5-2 and S-5-4, it can be seen that the increase in the concentration of additive has a direct effect on the wettability properties of sample S-5-4 and results in 46° increase in the contact angle in comparison with sample S-5-2; however, it reduces the advancing contact angle to 67°. These simultaneous increase and decrease in the static and advancing contact angles are dependent on the variations of surface tension. Sample S-5-4 represents a 33% drop in the surface tension relative to sample S-5-0. Comparison of the samples containing additive with respect to their additive contents reveals that at low and high additive concentrations, normal sample (S-0-2) and nanocomposite sample (S-5-4) have higher static contact angles, respectively. As previously mentioned, the wettability behavior of surface is governed by both the surface geometry and surface chemistry. The cause of lower surface tension, and consequently, the higher contact angle of the specimens coated in the electrolyte containing potassium stearate is the interaction between the substrate ions and the stearate ions and production of aluminum stearate. This leads to the lowering of the surface

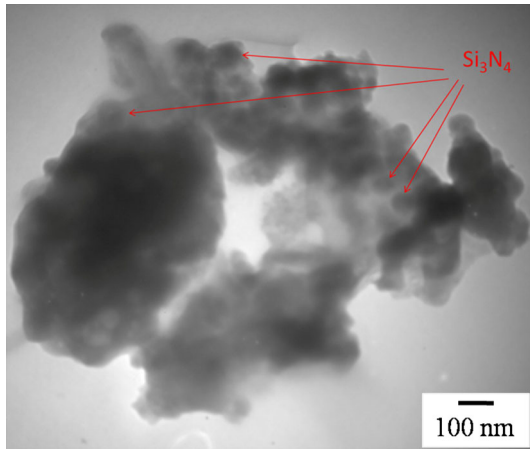


Fig. 4 TEM image from cross section of sample S-5-2

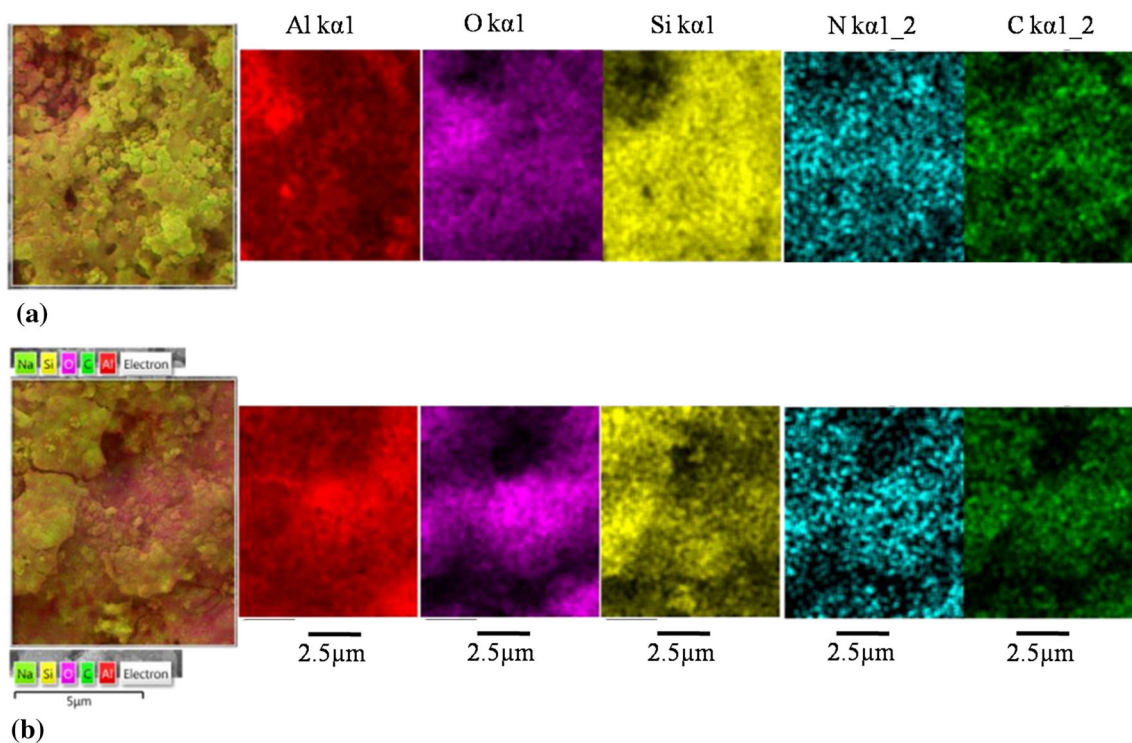


Fig. 5 EDS analyses of nanocomposite samples including (a) S-5-2 and (b) S-5-4

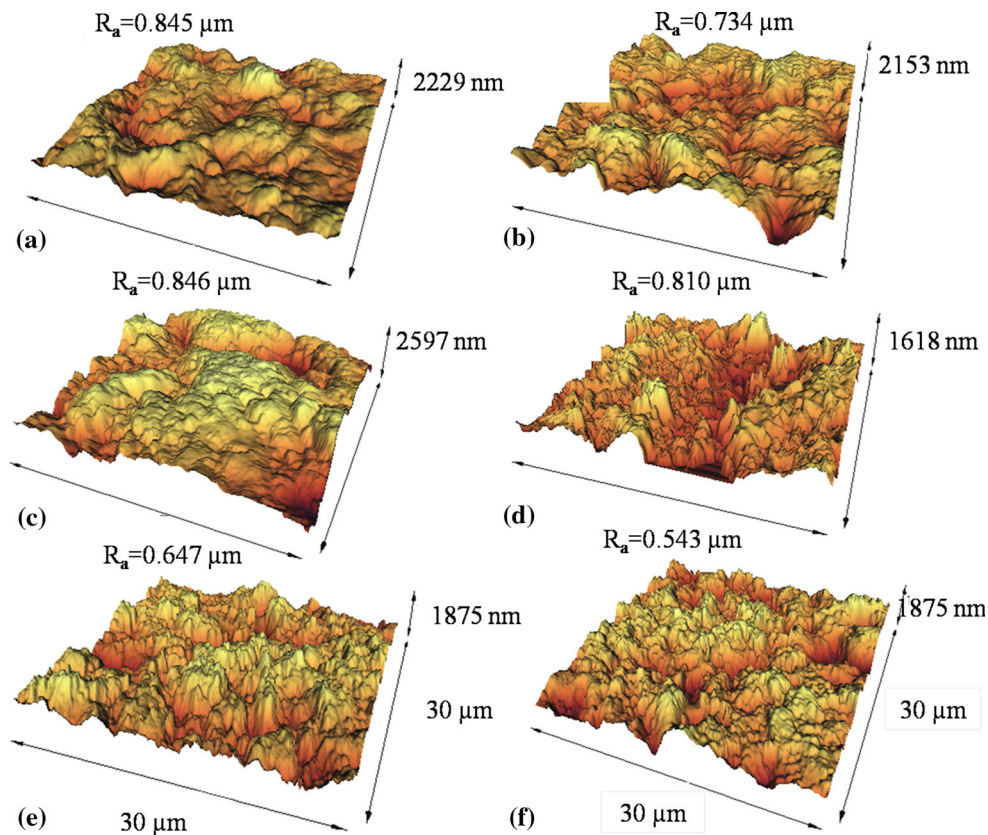


Fig. 6 AFM images from free surface of samples, showing (a) S-0-2, (b) S-0-4, (c) S-5-2, (d) S-5-4, (e) R-0-0, and (f) R-5-0

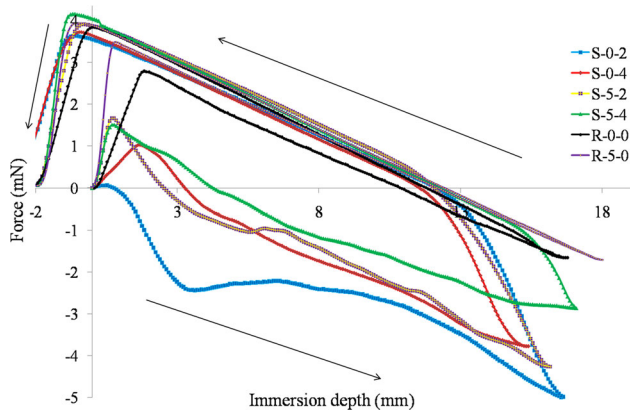


Fig. 7 Curves of Wilhelmy plate force vs. immersion depth for various samples

tension of the coating. FTIR test was used in order to confirm the presence of stearate chains and their bonding in the PEO coating. As shown in Fig. 8, in the obtained spectra, two peaks are seen in the range of 2923 cm^{-1} , which are attributed to the C-H stretching vibration. The presence of C-H bond in the FTIR test shows that a compound by this bond exists in the coating. The observed peak in the 1469 cm^{-1} is also attributed to the symmetric stretching vibrations of $-\text{CO}_2^-$ (Ref 48). These bonds belong to the stearate chains ($\text{CH}_3(\text{CH}_2)_{16}\text{COO}^-$) that are adsorbed on the coating surface and thus reduce the surface energy (Ref 49). Reaction between stearic acid and Al ions during the plasma electrolytic oxidation treatment leads to the formation of a compound between Al ions and stearate chains and its deposition on the PEO coating. This in turn leads to the formation of hydrophobic layer on the PEO coating by one-step treatment. Huang et al. (Ref 25) also used stearic acid in the electrolyte to fabricate one-step super-hydrophobic coating. They concluded that super-hydrophobicity of coating

Table 3 Contact angle values for different samples

Sample code	Contact angle	Contact angle hysteresis	Advancing contact angle	Receding contact angle	Surface tension, mN/m
S-0-2	65	51	90	39	26
S-0-4	40	43	79	36	34
S-5-2	39	46	77	31	35
S-5-4	46	38	67	28	43
R-0-0	6	10	41	32	61
R-5-0	6	4	34	31	65

is related to the reaction between copper and stearic acid solution and formation of copper stearate and therefore decrease in the surface tension of copper substrate. The reaction between stearic acid and substrate to form a low surface tension species is also addressed by Feng et al. (Ref 50).

3.5 Corrosion Behavior

Figure 9 illustrates the cyclic polarization curves of various samples, and Table 4 presents the extracted and calculated information from Fig. 9. Here, the pitting corrosion current is

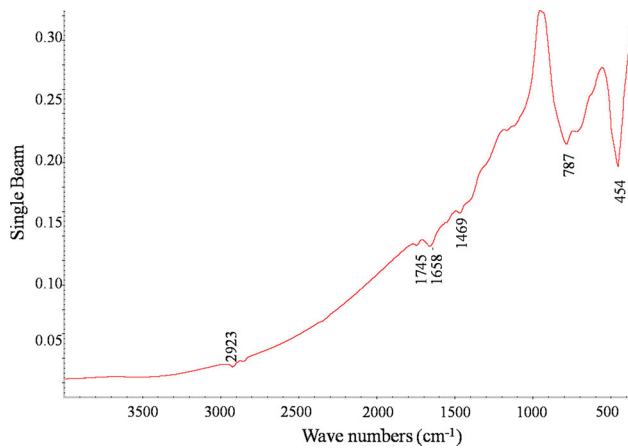


Fig. 8 FTIR spectrum of the S-0-2 coating

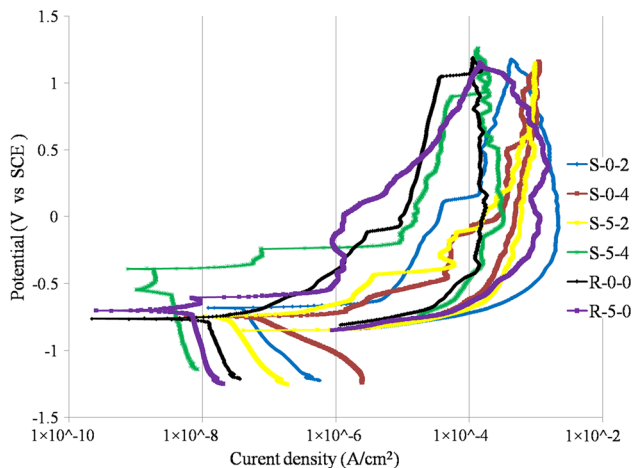


Fig. 9 Cyclic polarization curves of various samples

determined from the intersection between cathodic branch of the curve and corrosion potential of the reverse sweep branch (Ref 51). Comparison of samples R-0-0 and R-5-0 shows that the addition of nanopowder in the electrolyte reduces the corrosion rate of normal coating to 60% and its pitting corrosion rate to 45%. When polarization (anodic) increases, the current density slightly rises; while for others, the current density dramatically increased. This potential is called breakdown potential, and this behavior is referred to as breakdown of anodized layer. The anodic branch of sample R-0-0 has a slight slope, and no breakdown occurs up to the potential -0.14 V. Once again, by comparing samples R-0-0 and R-5-0, one can see that the presence of nanopowder in the electrolyte results in the drop of the breakdown potential of the coating to -0.6 V, so, at this potential, the corrosion current increases sharply because of pitting. Although these nanopowders reduce the corrosion rate, they make the coating more prone to failure and pitting formation during the polarization (at -0.6 V).

The corrosion results of samples S-0-2 and S-0-4 compared with that of sample R-0-0 show that the addition of potassium stearate to the electrolyte of normal coatings results in the failure of the coating at the beginning of anodic branch and 4-5 times rise in the corrosion rate for different concentrations. In this regard, the addition of potassium stearate to the electrolyte results in a 100-mV shift to more noble values in the corrosion potential of sample S-0-2 and a 30-mV shift to more noble values in the corrosion potential of sample S-0-4. However, the area under the curve of sample S-0-2 does not significantly change with the addition of potassium stearate, while the current in anodic branch is one decade more than that for the sample without additive, implying its higher pitting susceptibility. Besides, the pitting corrosion current becomes 4 times greater than that of sample R-0-0. Comparison of samples S-0-4 and R-0-0 indicates that their sweeping branches become closer though sample S-0-4 has a smaller area enclosed by the curve and low difference in the currents through two-way sweeping. Here, the pitting susceptibility is still high compared to the sample without additive, and the pitting corrosion current becomes 11 times larger than that of sample R-0-0. By comparing the corrosion results of samples S-5-2 and R-5-0, one may conclude that the addition of potassium stearate to the electrolyte of nanocomposite coatings at low concentrations causes 7.5 times increase in corrosion rate, and at the beginning of anodic branch leads to the coating failure. Although because of the high current in advancing branch, the difference in currents through the branches of two-way sweep is low (Ref 52-54), the pitting susceptibility is still high, and the pitting corrosion current is 4.6 times greater than that of sample R-5-0. By comparing the corrosion results of samples S-5-4 and R-5-0,

Table 4 Results of dynamic polarization test

Sample code	Corrosion current density, A/cm ²	Pitting current density, A/cm ²	Corrosion potential V vs. SCE	Breakdown potential V vs. SCE	Curve area	Current in maximum polarization, A/cm ²
S-0-2	4E-08	7E-08	-0.677	-0.673	2.3	4.24×10^{-4}
S-0-4	5E-08	2E-07	-0.736	-0.713	0.9	1.1×10^{-3}
S-5-2	3E-08	4E-08	-0.746	-0.714	1.2	9.68×10^{-4}
S-5-4	2E-09	5E-09	-0.542	-0.388	2.3	1.34×10^{-4}
R-0-0	1E-08	1.6E-08	-0.762	-0.142	2.4	1.20×10^{-4}
R-5-0	4E-09	8.7E-09	-0.700	-0.606	3.8	1.43×10^{-4}

it seems that the increase in concentration of potassium stearate results in a 50% drop in the corrosion rate of nanocomposite coating; it also shifts the breakdown potential to 0.2 V and the corrosion potential to 0.16 V into more noble values. The corrosion resistance of the coating depends on the properties of oxide film such as thickness and porosity, as well as the composition of aggressive environment (Ref 55); therefore, this improvement in the corrosion resistance is attributed to the reduced surface porosity. Considering the potential of reverse cycles for various samples, it is observed that the corrosion rate inside the pits is equal to the corrosion rate of samples; also, the pitting corrosion current exhibits a 40% drop compared to sample R-5-0.

4. Conclusion

The effect of potassium stearate addition on the microstructure, wettability and corrosion behavior of nanocomposite PEO coating was investigated. The results indicated that the addition of potassium stearate to the electrolyte reduced the spark initiation voltage during the coating process. The simultaneous effect of stearate chains deposition and nanopowders absorption in the coatings resulted in the intensified increase in the weight of samples. It was also found that both of the suspension ingredients, i.e., nanopowder and additive (potassium stearate), could reduce the surface porosity of the coatings by itself; also, the simultaneous effects of these two factors resulted in a severe drop in the surface porosity down to 1% as well as the surface roughness reduction. The addition of potassium stearate to the electrolyte resulted in a 50% drop in the surface tension and a 60° increase in the contact angle of the coating. The addition of potassium stearate to the electrolyte increased both the pitting and general corrosion rates of the coatings. Nanopowder suspension by forming a nanocomposite coating reduced the corrosion rate of the samples at any additive concentration. The simultaneous presence of nanopowder and high content of potassium stearate in the electrolyte resulted in the maximum drop of the corrosion and pitting rates.

References

- L. Minghua and T. Hikihara, A Coupled Dynamical Model of Redox Flow Battery Based on Chemical Reaction, Fluid Flow, and Electrical Circuit, *IEICE Trans. Fundam. Electron. Commun. Comput. Sci.*, 2008, **91**(7), p 1741–1747
- S.-S. Hsieh and C.-Y. Lin, Convective Heat Transfer in Liquid Microchannels with Hydrophobic and Hydrophilic Surfaces, *Int. J. Heat Mass Transf.*, 2009, **52**(1), p 260–270
- K. Liu and L. Jiang, Metallic Surfaces with Special Wettability, *Nanoscale*, 2011, **3**(3), p 825–838
- T.V. Charpentier et al., Development of Anti-icing Materials by Chemical Tailoring of Hydrophobic Textured Metallic Surfaces, *J. Colloid Interface Sci.*, 2013, **394**, p 539–544
- Y. Song et al., Adhesion and Friction Properties of Micro/nano-engineered Superhydrophobic/Hydrophobic Surfaces, *Thin Solid Films*, 2010, **518**(14), p 3801–3807
- L. Zhao et al., One-Step Method for the Fabrication of Superhydrophobic Surface on Magnesium Alloy and Its Corrosion Protection, Antifouling Performance, *Corros. Sci.*, 2014, **80**, p 177–183
- L. Cao, *Superhydrophobic Surface: Design, Fabrication, and Applications*, University of Pittsburgh, Pittsburgh, 2010
- S. He et al., Preparation and Properties of ZnO Nanostructures by Electrochemical Anodization Method, *Appl. Surf. Sci.*, 2010, **256**(8), p 2557–2562
- Y. Liang et al., Hydrophilic/Hydrophobic Behavior on Ti Foil Surface Prepared by Anodization, *Adv. Mater. Res.*, 2013, **602**, p 1659–1662
- I. Woodward et al., Micropatterning of Plasma Fluorinated Super-Hydrophobic Surfaces, *Plasma Chem. Plasma Process.*, 2006, **26**(5), p 507–516
- A. Hozumi, D.F. Cheng, and M. Yagihashi, Hydrophobic/Superhydrophobic Oxidized Metal Surfaces Showing Negligible Contact Angle Hysteresis, *J. Colloid Interface Sci.*, 2011, **353**(2), p 582–587
- S.S. Latthe et al., Superhydrophobic Silica Films by Sol-Gel Coprecursor Method, *Appl. Surf. Sci.*, 2009, **256**(1), p 217–222
- S. Wang, L. Feng, and L. Jiang, One-Step Solution-Immersion Process for the Fabrication of Stable Bionic Superhydrophobic Surfaces, *Adv. Mater.*, 2006, **18**(6), p 767–770
- D. Sarkar and N. Saleema, One-Step Fabrication Process of Superhydrophobic Green Coatings, *Surf. Coat. Technol.*, 2010, **204**(15), p 2483–2486
- H. Wang, D. Dai, and X. Wu, Fabrication of Superhydrophobic Surfaces on Aluminum, *Appl. Surf. Sci.*, 2008, **254**(17), p 5599–5601
- B. Yin et al., Novel Strategy in Increasing Stability and Corrosion Resistance for Super-Hydrophobic Coating on Aluminum Alloy Surfaces, *Appl. Surf. Sci.*, 2011, **258**(1), p 580–585
- Liu, W., et al., *Fabrication of The Superhydrophobic Surface on Aluminum Alloy by Anodizing and Polymeric Coating*, Applied Surface Science, 2012
- W.Y. Liu et al., Effects of Oxalic Acid and Sodium Chloride on the Superhydrophobic Surface on Aluminum Alloy by Anodizing and PP-Coating, *Adv. Mater. Res.*, 2012, **583**, p 338–341
- J. Li et al., Superhydrophobicity of Bionic Alumina Surfaces Fabricated by Hard Anodizing, *J. Bionic Eng.*, 2011, **8**(4), p 369–374
- M. Aliofkhaezai and A.S. Rouhaghdam, Study of Nanoparticle Adsorption in Single Discharge of Plasma Electrolysis, *Electrochem. Commun.*, 2012, **20**(1), p 88–91
- V. Rudnev et al., Fabrication of Polytetrafluoroethylene-and Graphite-Containing Oxide Layers on Aluminum and Titanium and Their Structure, *Russ. J. Phys. Chem. A*, 2013, **87**(6), p 1021–1026
- V. Rudnev et al., Formation of Oxide Layers Modified with Polytetrafluoroethylene or Graphite on Aluminum and Titanium Alloys by Plasma Electrolytic Oxidation, *Russ. J. Appl. Chem.*, 2012, **85**(8), p 1147–1152
- S. Gnedenkov et al., Formation and Electrochemical Properties of the Superhydrophobic Nanocomposite Coating on PEO Pretreated Mg–Mn–Ce Magnesium Alloy, *Surf. Coat. Technol.*, 2013, **232**, p 240–246
- S. Wang et al., Preparation of Superhydrophobic Silica Film on Mg–Nd–Zn–Zr Magnesium Alloy with Enhanced Corrosion Resistance by Combining Micro-arc Oxidation and Sol-Gel Method, *Surf. Coat. Technol.*, 2012, **213**, p 192–201
- Y. Huang, D. Sarkar, and X.-G. Chen, A One-Step Process to Engineer Superhydrophobic Copper Surfaces, *Mater. Lett.*, 2010, **64**(24), p 2722–2724
- R.M. Wu et al., Fabrication of a Super-Hydrophobic Micro-Nanoporous Aluminum Surface by Anodic Oxidation, *Appl. Mech. Mater.*, 2012, **200**, p 190–193
- T. Liu et al., Investigations on Reducing Microbiologically-Influenced Corrosion of Aluminum by Using Super-Hydrophobic Surfaces, *Electrochim. Acta*, 2010, **55**(18), p 5281–5285
- R.L. Bendure, Dynamic Adhesion Tension Measurement, *J. Colloid Interface Sci.*, 1973, **42**(1), p 137–144
- E. Chibowski, Surface Free Energy of a Solid from Contact Angle Hysteresis, *Adv. Coll. Interface Sci.*, 2003, **103**(2), p 149–172
- E. Matykina et al., Incorporation of Zirconia into Coatings Formed by DC Plasma Electrolytic Oxidation of Aluminium in Nanoparticle Suspensions, *Appl. Surf. Sci.*, 2008, **255**(5 PART 2), p 2830–2839
- E. Matykina et al., Optimisation of the Plasma Electrolytic Oxidation Process Efficiency on Aluminium, *Surf. Interface Anal.*, 2010, **42**(4), p 221–226
- S. Sarbishei, M.A. Faghihi Sani, and M.R. Mohammadi, Study Plasma Electrolytic Oxidation Process and Characterization of Coatings Formed in an Alumina Nanoparticle Suspension, *Vacuum*, 2014, **108**, p 12–19
- X. Guo et al., Experimental Study of Corrosion Protection of a Three-Layer Film on AZ31B Mg Alloy, *Corros. Sci.*, 2012, **65**, p 367–375

34. X. Guo et al., A New Nanoparticle Penetrant Used for Plasma Electrolytic Oxidation Film Coated on AZ31 Mg Alloy in Service Environment, *Surf. Coat. Technol.*, 2012, **206**(23), p 4833–4839
35. M. Aliofkhazraei and A.S. Rouhaghdam, Wear and Coating Removal Mechanism of Alumina/Titania Nanocomposite Layer Fabricated by Plasma Electrolysis, *Surf. Coat. Technol.*, 2011, **205**(SUPPL. 2), p S57–S62
36. E. Matykina et al., Incorporation of Zirconia into Coatings Formed by DC Plasma Electrolytic Oxidation of Aluminium in Nanoparticle Suspensions, *Appl. Surf. Sci.*, 2008, **255**(5), p 2830–2839
37. S.V. Gnedenkov et al., Protective Composite Coatings Obtained by Plasma Electrolytic Oxidation on Magnesium Alloy MA8, *Vacuum*, 2014, **120**, p 107–114
38. M. Sandhyarani et al., Fabrication, Characterization and In Vitro Evaluation of Nanostructured Zirconia/Hydroxyapatite Composite Film on Zirconium, *Surf. Coat. Technol.*, 2014, **238**, p 58–67
39. C.J. Hu and M.H. Hsieh, Preparation of Ceramic Coatings on an Al-Si Alloy by the Incorporation of ZrO₂ Particles in Microarc Oxidation, *Surf. Coat. Technol.*, 2014, **258**, p 275–283
40. Y.L. Song, X.Y. Sun, and Y.H. Liu, Effect of TiO₂ Nanoparticles on the Microstructure and Corrosion Behavior of MAO Coatings on Magnesium Alloy, *Mater. Corros.*, 2012, **63**(9), p 813–818
41. Y. Xiong et al., Degradation Behavior of n-MAO/EPD Bio-ceramic Composite Coatings on Magnesium Alloy in Simulated Body Fluid, *J. Alloy. Compd.*, 2015, **625**, p 258–265
42. W. Xu et al., Rapid Fabrication of Large-Area, Corrosion-Resistant Superhydrophobic Mg Alloy Surfaces, *ACS Appl. Mater. Interfaces*, 2011, **3**(11), p 4404–4414
43. A.M. Mohamed, A.M. Abdullah, and N.A. Younan, Corrosion Behavior of Superhydrophobic Surfaces: A Review, *Arab. J. Chem.*, 2015, **8**(6), p 749–765
44. M. Ma and R.M. Hill, Superhydrophobic Surfaces, *Curr. Opin. Colloid Interface Sci.*, 2006, **11**(4), p 193–202
45. X. Zhang et al., Superhydrophobic Surfaces: From Structural Control to Functional Application, *J. Mater. Chem.*, 2008, **18**(6), p 621–633
46. E. Chibowski and R. Perea-Carpio, Problems of Contact Angle and Solid Surface Free Energy Determination, *Adv. Coll. Interface Sci.*, 2002, **98**(2), p 245–264
47. H.-J. Butt, K. Graf, and M. Kappl, *Physics and Chemistry of Interfaces*, Wiley-VCH, New York, 2003
48. Y. Liu et al., Self-Assembled Monolayers on Magnesium Alloy Surfaces from Carboxylate Ions, *Appl. Surf. Sci.*, 2006, **252**(10), p 3818–3827
49. X.-J. Cui et al., Fabrication and Corrosion Resistance of a Hydrophobic Micro-arc Oxidation Coating on AZ31 Mg Alloy, *Corros. Sci.*, 2015, **90**, p 402–412
50. L. Feng et al., Superhydrophobic Alumina Surface Based on Stearic Acid Modification, *Appl. Surf. Sci.*, 2011, **257**(9), p 3959–3963
51. R.W. Revie, *Corrosion and Corrosion Control*, Wiley, New York, 2008
52. L. Escalera et al., Corrosion Characteristics of Al-Si-Mg/SiCp Composites with Varying Si/Mg Molar Ratio in Neutral Chloride Solutions, *Mater. Corros.*, 2009, **60**(9), p 683–689
53. A.S. Hamdy, F. Alfosail, and Z. Gasem, Eco-friendly, Cost-Effective Silica-Based Protective Coating for an A6092/SiC/17.5p Aluminum Metal Matrix Composite, *Electrochim. Acta*, 2013, **89**, p 749–755
54. Y. Liu, G.Z. Meng, and Y.F. Cheng, Electronic Structure and Pitting Behavior of 3003 Aluminum Alloy Passivated Under Various Conditions, *Electrochim. Acta*, 2009, **54**(17), p 4155–4163
55. G.B. Darband, A. Afshar, and A. Aliabadi, Zn–Ni Electrophosphating on Galvanized Steel Using Cathodic and Anodic Electrochemical Methods, *Surf. Coat. Technol.*, 2016, **306**, p 497–505